



**HAL**  
open science

# Retrieval of Mars surface physical properties from OMEGA hyperspectral images using Regularized Sliced Inverse Regression.

Caroline Bernard-Michel, Sylvain Douté, Laurent Gardes, Stéphane Girard

## ► To cite this version:

Caroline Bernard-Michel, Sylvain Douté, Laurent Gardes, Stéphane Girard. Retrieval of Mars surface physical properties from OMEGA hyperspectral images using Regularized Sliced Inverse Regression.. [Research Report] 2008, pp.43. inria-00276116v1

**HAL Id: inria-00276116**

**<https://inria.hal.science/inria-00276116v1>**

Submitted on 28 Apr 2008 (v1), last revised 6 Nov 2008 (v2)

**HAL** is a multi-disciplinary open access archive for the deposit and dissemination of scientific research documents, whether they are published or not. The documents may come from teaching and research institutions in France or abroad, or from public or private research centers.

L'archive ouverte pluridisciplinaire **HAL**, est destinée au dépôt et à la diffusion de documents scientifiques de niveau recherche, publiés ou non, émanant des établissements d'enseignement et de recherche français ou étrangers, des laboratoires publics ou privés.

# <sup>1</sup> Retrieval of Mars surface physical properties from <sup>2</sup> OMEGA hyperspectral images using Regularized <sup>3</sup> Sliced Inverse Regression

C. Bernard-Michel,<sup>1</sup> S. Douté,<sup>2</sup> L. Gardes,<sup>1</sup> and S. Girard<sup>1</sup>

---

C. Bernard-Michel, L. Gardes and S. Girard, MISTIS, INRIA Rhône-Alpes, Montbonnot, Inovalée, 655 avenue de l'Europe, 38 334 Saint Ismier Cedex, France.

S. Douté, Laboratoire de Planétologie de Grenoble, Bât. D de Physique, B.P. 53, 38041 Grenoble Cedex 9, France. (sylvain.doute@obs.ujf-grenoble.fr)

<sup>1</sup>MISTIS, INRIA Rhône-Alpes,  
Montbonnot, France.

<sup>2</sup>Laboratoire de Planétologie de Grenoble,  
Saint Martin-d'Hères, France.

4 **Abstract.** Hyperspectral remote sensing, also known as imaging spec-  
5 troscopy, is a promising space technology regularly selected by agencies with  
6 regard to the exploration and observation of planets, to earth's geology or  
7 to the monitoring of the environment. It allows to collect for each pixel of  
8 a scene, the intensity of light energy reflected from planets as it varies across  
9 different wavelengths. More than one hundred spectels in the visible and near  
10 infra-red are typically recorded, making it possible to observe a continuous  
11 spectrum for each image cell. Usually, in space exploration, the analysis of  
12 these spectral signatures allows to retrieve the physical, chemical or miner-  
13 alogical properties of surfaces and of atmospheres that may help to under-  
14 stand the geological and climatological history of planets.

15 We propose in this paper a statistical method to evaluate the physical prop-  
16 erties of surface materials on Mars from hyperspectral images collected by  
17 the OMEGA instrument aboard the Mars express spacecraft. The approach  
18 we develop is based on the estimation of the functional relationship  $F$  be-  
19 tween some physical parameters and observed spectra. For this purpose, a  
20 database of synthetic spectra is generated by a physical radiative transfer  
21 model and used to estimate  $F$ . The high dimension of spectra is reduced by  
22 using Gaussian regularized sliced inverse regression (GRSIR) to overcome  
23 the curse of dimensionality and consequently the sensitivity of the inversion  
24 to noise (ill-conditioned problems). Compared with a naive spectrum match-  
25 ing approach such as the  $k$ -nearest neighbors algorithm, estimates are more  
26 accurate and realistic.

## 1. Introduction

Visible and near infrared imaging spectroscopy is a key remote sensing technique to study and monitor planets. It allows the detection, mapping and characterization of minerals, as well as volatile species, that often constitute the first step toward the resolution of key climatic and geological issues [Murchie *et al.*, 2007; Bibring *et al.*, 2004a; Brown *et al.*, 2004; Carlson *et al.*, 1992]. These tasks are carried out by the spectral analysis of solar light reflected in different directions by the materials forming the top few millimeters or centimeters of the ground. Physical properties of the surface, such as chemical composition, granularity, texture, and physical state are some of the most important parameters that characterize the morphology of the hundred thousand spectra that typically constitute an image. Modeling the direct link between these parameters and observable spectra is usually called the forward problem in classical physics. It can be evaluated numerically by radiative transfer models, simulating the propagation of solar light through the atmosphere and surface to the sensor [Douté *et al.*, 2007; Shkuratov *et al.*, 1999; Douté and Schmitt, 1998; Hapke, 1993]. It allows us, for given values of the model parameters, to simulate the spectra that should be observed. Conversely, deducing the physical model parameters from the observed spectra is called an inverse problem. It generally cannot be solved analytically, and the use of optimization or statistical methods becomes necessary. From a general point of view, solving inverse problems requires that the fundamental physics are adequately understood, such that a function,  $G$ , may be specified between the spectra  $X$  and the parameters  $Y$  such that:

$$X = G(Y). \tag{1}$$

27 Once this relationship  $G$  is known, different methods can be used to deduce the parameters  
28  $Y$  from the observable  $X$ . They can be roughly divided in three categories (for further  
29 details and comparisons, see [*Kimes et al.*, 2000; *Pragnère et al.*, 1999]):

30 • *Optimization algorithms* are the most traditional approaches. They consist of min-  
31 imizing an objective function that expresses the similarity between an observed and a  
32 simulated spectrum. For example, this function may be the mean square errors function,  
33 where the errors are the differences between observed and simulated reflectances at each  
34 wavelength. These methods involve numerical optimization techniques (Powell's method,  
35 Simplex method, quasi-Newton method...) starting with an initial guess of the param-  
36 eters and searching for the optimum parameters via an iterative process that minimizes  
37 the objective function. In fact, estimations are unstable since inverse problems are often  
38 ill-posed (solutions are not unique and a small change in the data can lead to enormous  
39 differences in the estimations). A probabilistic formalism can then be used to regularize  
40 inverse problems by introducing a prior distribution on model parameters [*Aster et al.*,  
41 2005; *Tarantola*, 2005; *Mosegaard and Tarantola*, 2002]. These approaches are compu-  
42 tationally expensive since they iteratively simulate new spectra. Therefore, they cannot  
43 be applied in the case of the inversion of an image with several hundred thousand pix-  
44 els. Moreover, they can sometimes fall into local minima if the objective function is not  
45 convex.

46 • *Look-up table (LUT) / k-nearest neighbors approach (k-NN)*: In order to replace a  
47 heavy runtime computation with a simpler look-up operation, a large database (look-up  
48 table) is generated by radiative transfer for many parameter values and stored on disks.  
49 To inverse a hyperspectral image, the spectrum at each pixel is then compared with the

50 look-up table spectra in order to find the best match (the nearest neighbor), according to  
51 an objective function minimization. Parameters are then deduced from the look-up table  
52 best match spectrum [*Carlson et al.*, 2005; *Philpot et al.*, 2004; *Combal et al.*, 2002; *Weiss*  
53 *et al.*, 2000; *Douté et al.*, 2001]. In comparison with traditional optimization methods,  
54 the speed gain is significant, since retrieving a value from memory is often faster than  
55 undergoing an expensive computation. The main disadvantages of this approach are the  
56 multiplicity of solutions and their instability (see section 3).

- *Training approaches* assume that there exists a functional relationship

$$Y = F(X) \tag{2}$$

57 between spectra and parameters. This relationship corresponds to the inverse of the  
58 physical model  $G$  in the forward problem (1). The idea is to use a look-up table to  
59 estimate the underlying mathematical relationship  $F$ . This relationship then allows us to  
60 estimate the parameters of new spectra. Computation time can then be very competitive.  
61 Neural networks [*Kamgar-Parsi and Gualtieri*, 1990] or support vector machines (SVM)  
62 [*Scholkopf and Smola*, 2002] can be used to learn the function  $F$ . The advantage of a such  
63 a training approach is that, once the relationship has been established, it can be used for  
64 very large sets and for all new images with the same physical model.

65 Inverse problems occur in many branches of sciences such as geophysics, hydrology,  
66 medical imaging, pedology, remote sensing, astronomy or planetology. The choice of  
67 one methodology among the others is generally determined according to the degree of  
68 knowledge of the studied physical phenomenon. It is also determined by the quality  
69 and quantity of measurements. In geophysics or meteorology, probabilistic approaches  
70 combined to optimization techniques are most of the time preferred for the following main

71 reasons: the inverse problem can be linearized, observations are numerous and physicists  
72 do have an *a priori* about the parameters variations. In planetary sciences, massive inverse  
73 problems have only been tackled recently since they intervene in the last step of a physical  
74 study of the huge collections of hyperspectral images. Moreover, inverting hyperspectral  
75 imaging on planets has to be designed with the following constraints:

76 • Dealing with extremely large datasets and various modeling require simple and fast  
77 methodologies,

78 • Inverting high dimensional spectra comes up against the curse of dimensionality,

79 • Observed spectra always contain some noise.

80 In that context, LUT and training approaches are generally preferred since they are fast  
81 and allow to deal with non linear inverse problems:

82 • The LUT/ $k$ -NN methodology is currently used by physicists to study planetary bod-  
83 ies [*Carlson et al.*, 2005; *Philpot et al.*, 2004; *Weiss et al.*, 2000; *Douté et al.*, 2001]. It  
84 provides an instinctive, simple and fast way to retrieve the model parameters. A good  
85 match between a simulated and an observed spectrum also reinforces the idea that the  
86 chosen physical modeling is realistic. However, we will show in section 3 that LUT/ $k$ -NN  
87 approaches lead to very unstable estimates.

88 • Training approaches have been recently considered in the study of terrestrial vege-  
89 tation. Among them, neural networks [*Combal et al.*, 2002; *Pragnère et al.*, 1999] seem  
90 promising but the underlying learning process still remains time consuming. Since the  
91 study of Mars is not focused on a particular type of soil, many physical models are ex-  
92 plored, and a faster methodology is required. Support vector machines [*Durbha et al.*,

93 2007] could be used but their disadvantage is that they are difficult to interpret statisti-  
94 cally and physically.

95 In this paper, we propose to develop a new training approach: the Gaussian regularized  
96 sliced inverse regression (GRSIR). It is based on a dimension reduction technique: the  
97 sliced inverse regression [Li, 1991]. To the best of our knowledge, this method has never  
98 been used in the context of inverse problems in planetology. It has the advantage to be fast,  
99 stable, statistically and physically interpretable and can also help to select an appropriate  
100 look-up table for inversion. For the sake of validation, this approach is compared all along  
101 with the naive but currently used  $k$ -NN approach. In section 2, we first introduce the  
102 datasets we are working with. Then, the limits of the LUT/ $k$ -NN approach are discussed  
103 in section 3. The Gaussian regularized sliced inverse regression (GRSIR) [Bernard-Michel  
104 *et al.*, 2007b] is introduced and detailed in section 4. The choice of an appropriate look-  
105 up table is discussed in section 5. Two applications of GRSIR methodology are then  
106 presented:

- 107 • A validation on simulations, in section 6, allows to quantify the relevance of GRSIR  
108 according to two criteria,
- 109 • In section 7 the retrieval of some physical parameters for the south permanent polar  
110 cap of Mars: proportions of CO<sub>2</sub> ice, dust, water ice and grain sizes of CO<sub>2</sub> ice and water  
111 ice.

## 2. Data

112 The datasets used in the next sections can be divided in three categories: The hyper-  
113 spectral images observed on Mars, a look-up table simulated by radiative transfer models

114 according to the physical modeling of these images and a test data in order to quantify  
115 the estimates accuracy. In any case, these datasets consist of:

116 • Some spectra  $X \in \mathbb{R}^d$ , where  $d$  is the number of considered wavelengths and will be  
117 called the dimension of the problem. In the presented application  $d$  is equal to 184 and  
118 and consequently leads to the resolution of a high-dimensional problem.

119 • Some associated parameters  $Y \in \mathbb{R}^p$ , where  $p$  is the number of free parameters in  
120 the physical model. In this paper, five parameters ( $p = 5$ ) will be considered.

## 2.1. Hyperspectral Images from Mars

121 We concentrate on datasets collected by the spectro-imaging instrument: OMEGA  
122 (observatoire pour la minéralogie, l'eau, la glace et l'activité). OMEGA is one of the  
123 seven scientific instruments aboard the European spacecraft Mars express mission, sent  
124 in orbit around Mars in 2003. It has been developed by IAS and LESIA (Observatoire de  
125 Paris) with the support of CNES, and a participation of IFSI (Italy) and IKI (Russia).  
126 This visible and infrared mapping spectrometer should scan most of Mars from orbits in  
127 order to observe the gases and dust in the atmosphere and to look for signs of specific  
128 materials such as silicates, carbonates, ices at the surface. It records the visible and  
129 infrared light reflected from the planet in the wavelength range 0.5-5.2 microns and with  
130 a ground resolution varying from 350 m to 10 km. Our study will refer to three OMEGA  
131 hyperspectral images acquired during orbits 41, 61 and 103. They cover the high southern  
132 latitudes of Mars. The spatial resolution is about 2km per pixel and we considered 184  
133 wavelengths in the range 0.95-4.15. For each image, a preprocessing aiming at correcting  
134 the atmospheric gaseous contribution in the spectra has been applied [Douté *et al.*, 2007].  
135 After a first analysis, these OMEGA observations revealed [Bibring *et al.*, 2004b] that

136 the south polar region of Mars mainly contains water ice, carbon dioxide ice and dust. A  
137 detailed qualitative mapping of H<sub>2</sub>O and CO<sub>2</sub> ices during the local summer shows that  
138 the permanent south polar region is dominated by superficial CO<sub>2</sub> ice on the bright cap  
139 except at its edges where water ice appears in extended areas. Examining the coexistence  
140 modes (geographical or granular) between H<sub>2</sub>O, CO<sub>2</sub> ice and dust that best explain the  
141 morphology of the spectra has then led to the implementation of a physical modeling  
142 of individual spectra with a surface reflectance model [Douté *et al.*, 2007]. This model  
143 allows the generation of synthetic spectra with the corresponding pairs of parameters that  
144 constitute a look-table [Douté *et al.*, 2007]. We will focus on the terrain unit of strong  
145 concentration of CO<sub>2</sub>: the bright permanent south polar cap. This unit has been carefully  
146 mapped by a classification method based on wavanglets [Schmidt *et al.*, 2007]. For each  
147 image, the CO<sub>2</sub> ice areas contain about 10000 to 20000 spectra.

## 2.2. Look-up table

148 Because we do not have any *a priori* about the range of values in which each parameter  
149 is varying, we chose to simulate a large look-up table, containing parameters values that  
150 are probably not found in our three considered images. The look-up table has been  
151 simulated for five parameters varying spatially: the grain sizes of water and CO<sub>2</sub> ices, the  
152 proportions of water ice, CO<sub>2</sub> ice and dust. The sum of the proportions is constrained to  
153 one. The other parameters intervening in the physical model, such as the incidence and  
154 emergence angles or the grain size of dust have been fixed to a constant. Details about  
155 the sampling strategy are given in Table 1. We will denote by:

- 156 •  $n$  the number of simulated spectra ( $n = 31500$ ),
- 157 •  $x_i \in \mathbb{R}^d, i \in \{1, \dots, n\}$  the spectra,

158 •  $y_i \in \mathbb{R}^p, i \in \{1, \dots, n\}$  the  $p$  associated parameters.

### 2.3. Test data

159 For the validation, the use of a test dataset is required that we will denote by "Tdata".  
160 The one we chose has been simulated by radiative transfer modeling for random values of  
161 the proportions of dust and CO<sub>2</sub> ice and the grain sizes of CO<sub>2</sub> and water ices. They have  
162 been simulated according to the same physical model than the one used for generating  
163 the look-up table. Details about the ranges of variation can be found in Table 1. In  
164 order to work in realistic conditions, a multiGaussian noise of dimension 184 has been  
165 added to all the spectra of the test dataset. The noise has been simulated with a mean  
166 fixed to zero for all wavelengths and with a covariance matrix determined experimentally  
167 from the OMEGA image acquired during orbit 41. A small portion of the image, very  
168 homogeneous in terms of composition and physical properties, is chosen so that we can  
169 assume that much of the variability comes from the noise. The latter is then evaluated  
170 by a statistics after applying a shift difference on the selected portion. Afterward, we will  
171 denote:

172 •  $n_T$  the number of spectra from Tdata ( $n_T = 3500$ ),

173 •  $x_i^T \in \mathbb{R}^d, i \in \{1, \dots, n_T\}$  the spectra from Tdata,

174 •  $y_i^T \in \mathbb{R}^p, i \in \{1, \dots, n_T\}$  the associated parameters.

### 3. Limits of the $k$ -NN approach

Let  $o \in \mathbb{R}^d$  be the spectral reflectance of one observed pixel on Mars.

The nearest neighbor algorithm (also known as the  $k$ -NN algorithm) consists of searching the  $k$  nearest spectra of  $o$  in the learning database minimizing the mean square errors

between the observed spectrum  $o$  and the simulated spectra. The  $k$  nearest spectra of the learning database are selected by sorting in ascending order the values of the objective function  $\Phi(i)$  defined by:

$$\Phi(i) = \|o - x_i\|^2. \tag{3}$$

175 where  $i \in \{1, \dots, n\}$ .

176 If  $k = 1$ , the estimated parameters for the pixel are then the ones associated to the nearest  
177 spectrum selected in the learning database. If  $k$  is greater than 1, then one can choose to  
178 estimate parameters by the mode, or the mean of the  $k$  best matches, but also to keep all  
179 the possible estimates. Most of the time, only the best match is retained.

180

181 The problem of  $k$ -NN approach is that it usually leads to very unstable estimates and  
182 it is then difficult to choose a judicious  $k$ . Let us consider the example of two spectra  
183 S1 and S2 for which parameters are known and let us add a reasonable noise to these  
184 spectra. Applying the  $k$ -NN methodology ( $k = 1$ ) leads to estimations given in Table 2.  
185 We can notice here that estimation errors are relatively small for spectrum S1 whereas  
186 they are much greater for spectrum S2. One first thinks that a good idea to improve  
187 results would be to consider more than 1 neighbor. In fact, figure 1 shows how unstable  
188 the estimates are. It presents the relative estimation error as a function of  $k$ , where  $k$  is  
189 the  $k$ th neighbor. First, we can see that considering the  $k$ th neighbor or the  $(k + 1)$ th  
190 neighbor generally leads to very different estimations. Moreover, for spectrum S1, errors  
191 are increasing when  $k$  is increasing whereas for spectrum S2 errors are decreasing when  $k$   
192 is increasing. That means that for spectrum S1, very few neighbors would be necessary  
193 to estimate the parameters properly whereas with spectrum S2, a lot of neighbors would

194 be required. In fact, for spectrum S2, more than one hundred neighbors are necessary  
195 to have at least a realistic estimation of the grain size of CO<sub>2</sub> ice. In these conditions,  
196 one can see that estimating parameters by a  $k$ -NN approach can lead to significant errors  
197 especially when there is no *a priori* on the solutions.

#### 4. Proposed approach

198 We propose here to estimate the functional relationship  $F$  between the spectra  $X \in \mathbb{R}^d$   
199 and each physical parameter  $Y^j = F(X) \in \mathbb{R}$  with  $j \in \{1, \dots, p\}$ . Since each parameter  
200 is studied individually, we will consider in the next sections that  $p = 1$  and we will always  
201 omit  $j$  for the sake of simplicity. Because of the curse of dimensionality, estimating a  
202  $d$ -variate function from the data is not realistic and dimension reduction techniques have  
203 to be applied. They rely on the assumption that the predictor  $X$  can be replaced by its  
204 projection onto a subspace of smaller dimension  $L$ , called the effective dimension reduction  
205 space (EDR), without loss of information. Denoting by  $\beta_1, \dots, \beta_L$  the basis of this sub-  
206 space, the functional relationship  $Y = F(X)$  can be rewritten as  $Y = f(\beta_1^t X, \dots, \beta_L^t X)$   
207 where  $f$  is now a  $L$ -variate function. In most applications,  $L$  is smaller than 3 making the  
208 estimation of  $f$  realistic. The estimation of the projection axes  $\beta_1, \dots, \beta_L$  is discussed in  
209 the next paragraph.

##### 4.1. Dimension reduction step: Gaussian regularized sliced inverse regression

Principal component analysis (PCA) is the most current technique that could be used  
to choose the  $\beta_i$ 's [Bishop, 2006, chapter 12]. The basic idea in PCA is to define the  
orthogonal projection of the spectra onto a lower dimensional linear space such that the  
total variance of the projected spectra is maximized. It amounts to diagonalizing the

spectra covariance matrix

$$\Sigma = \frac{1}{n} \sum_{i=1}^n (x_i - \bar{x})(x_i - \bar{x})^t \text{ where } \bar{x} = \frac{1}{n} \sum_{i=1}^n x_i \quad (4)$$

210 or equivalently to calculating the eigenvectors of  $\Sigma$ . However, in the case of a regres-  
211 sion problem, PCA is generally not satisfying since only the explanatory variables  $X$  are  
212 considered and the dependent variable  $Y$  is not taken into account. Specific dimension  
213 reduction techniques have been developed for regression problems, and among them Sliced  
214 Inverse Regression (SIR) is the most popular [Li, 1991]. It consists first of sorting the  
215 parameter values in increasing order and to divide them into a chosen number  $H$  of non  
216 overlapping slices  $S_h, h \in \{1, \dots, H\}$ . For each slice  $S_h$ , a mean spectrum  $m_h$  is calcu-  
217 lated by averaging the spectra for which the parameter values are varying in the slice (see  
218 equation (5)). The basic idea in SIR is then to define the orthogonal projection of the  
219 mean spectra onto a lower dimensional linear space such that the variance of the projected  
220 mean spectra is maximized under the constraint that the total projected variance is 1. It  
221 amounts to diagonalizing  $\Sigma^{-1}\Gamma$  where  $\Gamma$  is the mean spectra covariance matrix given in  
222 equation (6). This principle is illustrated on figure 2 showing that GRSIR consists of max-  
223 imizing the between-slice variance of the reduced spectra or equivalently in minimizing  
224 the within-slice variance.

Since inverse problems are generally ill-posed [Aster *et al.*, 2005; Tarantola, 2005],  $\Sigma$  is ill-conditioned making its inversion difficult. We thus propose to compute a Gaussian regularized version of Sliced Inverse Regression (GRSIR). Theoretical details can be found in [Bernard-Michel *et al.*, 2007a]. The concept of this method is to incorporate some prior information on the projections in order to dampen the effect of the noise in the input data, and to make the solution more regular or smooth. The ill-posed problem is then

replaced by a slightly perturbed well-posed problem that depends on a parameter  $\delta$ , called the regularization parameter. Similarly, GRSIR consists of computing the  $L$  eigenvectors corresponding to the  $L$  largest eigenvalues of  $(\Sigma^2 + \delta I_p)^{-1} \Sigma \Gamma$  where  $I_p$  is the  $d \times d$  identity matrix. In practice, GRSIR then requires the four following computational steps:

**Step 1:** Sorting  $y_i, i \in \{1, \dots, n\}$  in increasing order and dividing them into  $H$  non overlapping slices  $S_h, h = 1, \dots, H$ . If the Look-up table has been simulated for random values of  $Y$ , then the slices are chosen such that each slice contains the same number of observations. If the look-up table has been simulated for a fixed number of distinct parameters, slices are these distinct values.

**Step 2:** Computing the slice means. For each slice:

$$m_h = \frac{1}{n_h} \sum_{y_i \in S_h} x_i \quad (5)$$

where  $n_h$  denotes the number of observations in the slice  $S_h$ .

**Step 3:** Computing the "between slices" means covariance matrix:

$$\Gamma = \sum_{h=1}^H \frac{n_h}{n} (m_h - \bar{x})(m_h - \bar{x})^t \quad (6)$$

**Step 4:** Estimating the GRSIR axes  $\beta_1(\delta), \dots, \beta_L(\delta)$  by computing the eigenvectors of  $(\Sigma^2 + \delta I_p)^{-1} \Sigma \Gamma$ . The first GRSIR axis  $\beta_1(\delta)$  is determined by the eigenvector corresponding to the largest eigenvalue, the second GRSIR axis  $\beta_2(\delta)$  is determined by the eigenvector corresponding to the second largest eigenvalue and so on.

In section 6.3, we will give a criterion to choose the dimension  $L$ . We will see that in practical cases, only the first GRSIR axis is sufficient to retrieve parameters. Let us notice that this first axis can be viewed as a weight function of the wavelengths, giving

233 some important weights to the wavelengths that carry much more information about the  
 234 parameter. Afterward, we will denote by reduced spectra the projections of the spectra  
 235 on this axis  $\beta_1(\delta)$ .

## 4.2. Estimation of the functional relationship

236 Once a relationship has been revealed between reduced spectra and the parameter (see  
 237 for example figure 2), then the question comes to estimate this relation  $f$ . We propose to  
 238 use a piecewise linear interpolation on the set of data points  $(m_h^{proj}, m_h^{param}), h = 1, \dots, H$   
 239 where  $H$  denotes the number of slices  $S_h$ ,  $m_h^{proj} = \langle x_i, \beta_1(\delta) \rangle$  denotes the average of the  
 240 projection of the spectra  $x_i, y_i \in S_h$  for slice  $S_h$  and  $m_h^{param} = \frac{1}{n_h} \sum_{y_i \in S_h} y_i$  denotes the  
 241 average parameter value for slice  $S_h$ .

242 For each new spectrum  $x$  with a projection  $t = \langle \beta_1(\delta), x \rangle$ , the estimated parameter  
 243 value  $\hat{y}$  is then given by:

$$\hat{y} = \begin{cases} m_1^{param} & \text{if } t \in ] - \infty, m_1^{proj} ] \\ \sum_{h=1}^{H-1} \left[ m_h^{param} + (t - m_h^{proj}) \left( \frac{m_{h+1}^{param} - m_h^{param}}{m_{h+1}^{proj} - m_h^{proj}} \right) \right] & \text{if } t \in ] m_h^{proj}, m_{h+1}^{proj} ] \\ m_H^{param} & \text{if } t \in ] m_H^{proj}, +\infty [ \end{cases}$$

244 An example of the application of GRSIR to the look-up table is given in Figure 2. It  
 245 shows the relationship between reduced spectra and the grain size of CO<sub>2</sub> ice and its  
 246 estimation by a linear interpolation.

## 5. Choice of the Look-up table

247 In the simulated look-up table, we can imagine that many spectra are not necessary  
 248 to estimate properly the parameters of an observed image. For example, if the studied  
 249 image is the test data Tdata, we should remove from the look-up table all the spectra  
 250 with parameters values that are not included in the range of values of Tdata's parameters.

251 We would then obtain a new look-up table that leads to better estimations for both  $k$ -  
252 NN and GRSIR [*Bernard-Michel et al.*, 2007a]. The difficulty is that in practical cases,  
253 we do not have any *a priori* about the range of variations of the parameters. The best  
254 approach in that case is then to take a huge look-up table and to reduce it after the first  
255 estimations by GRSIR or  $k$ -NN. This approach suffers from the fact that if the database  
256 is too important, then estimations are strongly deteriorated. In the case of  $k$ -NN, these  
257 deteriorations are due to the similarity of some spectra with very different parameters  
258 that lead to multiple solutions. In the case of GRSIR, these deteriorations are mainly  
259 due to the spectra that are on the opposite too different from the observed one. In  
260 order to visualize the adequacy of the chosen look-up table with the observed spectra,  
261 we propose to use principal component analysis. We consider that we can retrieve the  
262 parameters of the observed spectra from a look-up table only if their projections on the  
263  $m$  first PCA axes (deduced from the application of PCA to the look-up table) coincide  
264 with the projection of the look-up table itself. For the sake of visibility and because in  
265 our applications two components explain until 88% of the total variance, we chose  $m = 2$ .  
266 In some cases, a greater value for  $m$  could be required. To select the most appropriate  
267 spectra for inversion in the look-up table, our idea is to retain the spectra from the look-  
268 up table whose projections on PCA axes are close to projections of the spectra from  
269 the observed image. In the plane spanned by the  $m$  first PCA axes, we calculate the  
270 distance of each projected spectrum from the look-up table with its nearest neighbor in  
271 the observed image. The histogram of these distances allows to distinguish a mixture of  
272  $n_{class}$  Gaussian densities  $\mathcal{N}(\mu_i, \Sigma_i)$  characterized by parameters such as the proportions  
273 of the mixture  $\pi_i, i \in \{1, \dots, n_{class}\}$ , the expectation  $\mu_i$  and the covariance matrix  $\Sigma_i$

274 of each class  $i, i \in \{1, \dots, nclass\}$ . The number of classes is chosen by the user and  
275 the parameters can be estimated by the Expectation-Maximization algorithm (EM) after  
276 being initialized randomly or by the K-means algorithm (for further details about mixture  
277 models and EM, see *Bishop* [see 2006, chapter 9]). Roughly summarizing, EM algorithm  
278 is a simple iterative optimization process for computing the maximum likelihood estimates  
279 of the parameters. One can then calculate and maximize the posterior probability that a  
280 spectrum belongs to a class observing the distances. This leads to a classification of the  
281 spectra into  $nclass$  classes, generally two classes: the class of spectra from the look-up  
282 table that are far from the observed spectra, and conversely the class of spectra that are  
283 close. A statistics calculated separately for the spectra belonging to each class allows to  
284 refine the estimation of  $\pi_i, \mu_i$ , and  $\Sigma_i, i \in \{1, \dots, nclass\}$ . An example is given in Figure  
285 3 with the image observed from orbit 41. The histogram allows to distinguish 3 classes  
286 from which the third class corresponds quite well to the class we are looking for.

287 We can also notice that some of the observed spectra are outside the projected look-up  
288 table. We can wonder if we should keep these spectra for the inversion step, because either  
289 the simulated look-up table is too small, or the chosen physical model is not relevant for  
290 them. We propose to select and remove these spectra using the previous methodology. In  
291 the PCA plane, the histogram of the distance of each observed spectrum with its nearest  
292 neighbor in the selected sub-look-up table allows to distinguish two classes: the invertible  
293 spectra and the non invertible spectra (figure 3). The non invertible spectra correspond  
294 to pixels at the boundary of the CO<sub>2</sub> bright area and we can then suppose that another  
295 physical model should be used to inverse them. Other examples can be found in the work

296 of *Bernard-Michel et al.* [2007a]. It is also shown that, on simulations, estimations are  
297 more accurate when applying such a selection.

## 6. Analyzing results on simulations

298 In this section, we propose to quantify the accuracy of GRSIR estimations by using  
299 the test data presented in section 2. We also show how to choose the regularization  
300 parameter and the EDR dimension. At last, results are presented comparing GRSIR and  
301  $k$ -NN methods.

### 6.1. Validation criteria

302 To assess the relevance of GRSIR methodology, we focus on two aspects of the valida-  
303 tion: the accuracy of the estimates and the quality of the relationship between reduced  
304 spectra and parameters. To this end, we define two validation criteria. The first one,  
305 denoted Normalized Root Mean Square Errors (NRMSE), quantifies the importance of  
306 estimation errors, that are the differences between the estimations  $\hat{y}_i^T$  and the real values  
307  $y_i^T$ . The second one, denoted SIR Criterion (SIRC) is the ratio between the "between-  
308 slices" variance of GRSIR projections and the total variance. It quantifies the quality  
309 of the relationship between projected spectra and parameters. A third validation crite-  
310 rion that could have been introduced is the RMSE between the test spectrum  $x_i^T$  and  
311 the spectrum that can be reconstructed by running the radiative transfer model with the  
312 estimated parameters. However, this criterion would have faced the ill-posed problem  
313 that two spectra can be very close in terms of RMSE even with very different parame-  
314 ters values. The consequences are that a good reconstruction does not always mean that  
315 parameters are well estimated.

The Normalized Root Mean Square Errors (NRMSE) criterion is defined as:

$$NRMSE = \sqrt{\frac{\sum_{i=1}^{n_T} (\hat{y}_i^T - y_i^T)^2}{\sum_{i=1}^{n_T} (y_i^T - \bar{y}^T)^2}} \text{ with } \bar{y}^T = \frac{1}{n_T} \sum_{i=1}^{n_T} y_i^T.$$

317 This measure is invariant with respect to position and scale and therefore it is possible to  
 318 deduce if one parameter is better estimated than another. The NRMSE is close to zero  
 319 when the predicted values are accurate and conversely becomes larger when predictions  
 320 are poor.

### 321 **6.1.2. the SIRC**

The SIR criterion for an axis  $\beta_\ell(\delta)$  is defined as the ratio between the "between-slices"  
 variance  $\beta_\ell^t(\delta)\Gamma\beta_\ell(\delta)$  of the projections of  $x_i, i \in \{1, \dots, n\}$  on  $\beta_\ell(\delta)$  and the total variance  
 $\beta_\ell^t(\delta)\Sigma\beta_\ell(\delta)$  of these same projections:

$$SIRC = \frac{\beta_\ell^t(\delta)\Gamma\beta_\ell(\delta)}{\beta_\ell^t(\delta)\Sigma\beta_\ell(\delta)} \quad (7)$$

322 It indicates the quality of the functional relationship between projections of the spectra  
 323 on the  $\ell$ th GRSIR axis and the parameters. In the SIR criterion, the total variance can  
 324 be interpreted as the sum of the between slices variance and the within slice variance. In  
 325 this case, one can see the quality of the relationship is perfect when the within variance  
 326 is close to zero, or equivalently when SIRC is close to 1. Finally, the closer SIRC is to 1,  
 327 the better the relationship is.

## **6.2. Choice of the regularization parameter**

328 In the case of Regularized Sliced Inverse Regression, estimations  $\hat{y}_i^T$  and consequently  
 329 NRMSE criterion as well as the SIRC score depend on a regularization parameter  $\delta$ .

330 When the regularization parameter increases, the functional relationship between pro-  
331 jected spectra and parameters is getting worse and consequently estimation errors are  
332 increasing. From another point of view, if the regularization parameter is too small, then  
333 estimation errors are huge in presence of noise because we are dealing with an ill-posed  
334 problem. So, there is a compromise to reach between deteriorating the functional rela-  
335 tionship and improving estimations by regularizing. In fact, this compromise lies in the  
336 choice of the regularization parameter. We propose here to choose this regularization  
337 parameter, for each parameter individually, minimizing the NRMSE criterion calculated  
338 between the parameter values from a test data and their estimations. The test data can  
339 be the look-up table itself spoiled by a multiGaussian noise supposed representative of the  
340 one affecting the OMEGA hyperspectral images. Let us notice that if there is no noise  
341 in the data, or in other words, if the observed data exactly corresponds to spectra that  
342 could be simulated by radiative transfer model, then no regularization is required and  
343 minimizing the NRMSE criterion for GRSIR would yield a value  $\delta$  close to zero. Figure  
344 4 shows how the choice of the regularization parameter changes according to the noise:

- 345 • the stronger the noise is, the greater the NRMSE are,
- 346 • when the noise is increasing, the chosen regularization parameter, that corresponds  
347 to the minimum of the NRMSE, is also increasing.

348 One can easily see that making a mistake on the estimation of the noise leads to a  
349 mistake in the estimation of the regularization parameter and consequently can lead to  
350 much more uncertain estimations.

### 6.3. Choice of the EDR dimension

351 In order to choose the EDR dimension, we propose to calculate the SIRC for each GRSIR  
352 axis  $\beta_\ell(\delta)$  with  $\ell \in \{1, \dots, d\}$ . As  $\ell$  is increasing, the SIRC decreases very rapidly and is  
353 almost zero after very few iterations of the index  $\ell$ . In the next sections, we will fix the  
354 dimension of the EDR to the index  $L$  from which the SIRC is significantly decreasing. For  
355 example, If we apply GRSIR to the look-up table, the SIRC calculated for the proportion  
356 of CO<sub>2</sub> ice on the first GRSIR axis is 0.985. This SIRC, very close to one, indicates that  
357 the relationship of interest is well revealed by the first axis. Calculated with the second  
358 axis, the SIRC drops to 0.1799 and then is close to zero for other axes. In this case,  
359 we will consider that taking into account these axes in the regression step do not bring  
360 sufficient information and is not necessary, and will fix the EDR dimension to one. In  
361 fact, analyzing the SIRC for all parameters and for two different physical models reveals  
362 that only one dimension is sufficient to retrieve the model parameters. We found only one  
363 situation for which two GRSIR axes have to be kept: the thickness of the compact slab of  
364 nearly pure CO<sub>2</sub> ice making the seasonal deposits of the south pole of Mars during spring  
365 [*Douté et al.*, 2008]. For this parameter, the SIRC is 0.89 for the first axis, 0.81 for the  
366 second axis and close to zero for the third one. Because the necessity to keep more than  
367 one GRSIR axis seems rare,  $L$  is set to one in the next sections.

#### 6.4. Analyzing the GRSIR axis

368 The spectral variability of the individuals  $x_i$  constituting the look-up table results from  
369 a complex interplay of the different input parameters  $y_i$  of the model. In particular two  
370 parameters can have a similar influence on the spectra for a certain range of values. As a  
371 consequence it is crucial to understand how the GRSIR method can untangle the depen-  
372 dencies in order to find independent one to one functional relationships between spectra

373 and parameters. We thus try to correlate each axis  $\beta_1(\delta)$  - which is a vector of spectral  
374 weights - and the variability specifically induced by the variation of the corresponding  
375 physical parameter. The other parameter values are kept constant at mean values. The  
376 weights are individually applied to very different level of reflectance depending on wave-  
377 length when calculating the reduced spectrum  $\beta_1^t x_i$ . Hence we find it more illustrative  
378 to represent the componentwise multiplication (wavelength by wavelength) of each axis  
379 with a representative spectrum. An illustration is given in figure 5 for the grain size of  
380 CO<sub>2</sub> ice. Additionally we overplot in figure 6 the absolute value (for the sake of clarity) of  
381 the proportions of water ice and dust and of the grain sizes of water and CO<sub>2</sub> ice. From  
382 our analysis we make the following observations: (i) The criteria applied when seeking an  
383 axis (maximizing the between-slice variance while minimizing the within-slice variance)  
384 implies that GRSIR does put weight on key spectral points that do not display necessary  
385 the highest variability when we change the value of the corresponding parameter. (ii) In  
386 the case of the physical model that we consider in this paper (intimate mixture of H<sub>2</sub>O,  
387 CO<sub>2</sub>, and dust), the spectral range from 0.92 to 2.75 microns is the most determinant  
388 for evaluating the parameters. (iii) The axis for H<sub>2</sub>O abundance, dust abundance, and  
389 grain size of CO<sub>2</sub> ice are quite similar: we have a strong weight put on wavelength 1.43  
390 micron (the bottom of a very reliable and narrow CO<sub>2</sub> ice absorption band) and, to a  
391 lesser extent, on the interval between 1.47 and 1.54 microns (H<sub>2</sub>O ice feature), and on  
392 wavelengths 1.87 and 2.29 microns (weak CO<sub>2</sub> ice bands but very distinct). Besides the  
393 three axes have in common a moderate value at 2.00 microns, at the bottom of a strong  
394 CO<sub>2</sub> ice band. The latter is not very diagnostic because it often saturates. Thus, it is  
395 satisfying that GRSIR does not put too much emphasis on it. The three axes also shows

396 differences that allow differentiation between the functional relationships. A relatively  
397 strong weight at 2.38 microns on the right wing of the 2.34 micron band is a specificity of  
398 the proportion of water ice. We can note in figure 5 that the reflectance at this wavelength  
399 is greatly variable when water ice abundance or CO<sub>2</sub> ice grain size varies. The axis for the  
400 proportion of dust stresses very much the variation of the spectrum continuum around 1  
401 micron and 1.77 micron that indeed strongly changes with dust concentration. No other  
402 parameter affects so much the continuum. The axis for the proportion of dust minimizes  
403 the influence of the small plateau at 2.62 microns contrary to the axis for the grain size  
404 of CO<sub>2</sub> ice. This is the solution GRSIR finds to differentiate axes of the proportion of  
405 dust and the grain size of CO<sub>2</sub> ice because the plateau level varies very much with both  
406 dust concentration and CO<sub>2</sub> ice grain size. Furthermore the axis for grain sizes of CO<sub>2</sub>  
407 ice induces less sensitivity to the spectrum continuum than the axis for the proportion  
408 of dust. In addition, it does not put a noticeable weight on the right wing of the 2.34  
409 micron band contrary to the axis for the proportion of water ice. (iv) Axis 5 which is  
410 linked to H<sub>2</sub>O grain size is very different from the others since it emphasizes, on the one  
411 hand, the continuum level around 1 micron, but not around 1.75 microns and, on the  
412 other hand, it emphasizes the whole spectral range between 2.35 and 2.65 microns. The  
413 principal conclusions we can draw from our study is that, at least for the model presented  
414 in this paper, the GRSIR method succeeds in decorrelating the evaluation of the differ-  
415 ent parameters. Indeed it has the ability to find a unique set of wavelengths where the  
416 variability of the spectrum is the most pertinent (but not necessary the highest) for the  
417 evaluation of a given parameter. One must note that these key wavelengths not only fall  
418 on the bottom of specific absorption bands for both H<sub>2</sub>O and CO<sub>2</sub> ices but also on specific

419 parts of the continuum as well as on specific band wings. The GRSIR method thus reveals  
420 and uses all the pertinent information contained in the spectra that allows to estimate  
421 the parameters. This information is more complete than if we were focusing only on band  
422 depths as one could expect in the first place. Finally, knowing at the key wavelengths  
423 the characteristics (signal to noise ratio, accuracy of the absolute radiometric calibration,  
424 etc.) of the instrument that acquires the spectra (the imaging spectrometer OMEGA in  
425 our case) is crucial to assess the quality of the solutions.

## 6.5. Results

426 In this section, we finally compare the naive  $k$ -NN approach with the GRSIR method-  
427 ology on the test data Tdata. We quantify the gain of one approach from the other  
428 according to the SIRC and NRMSE criteria but we also compare estimations to real val-  
429 ues with the help of graphic tools such as scatter plots or histograms. For both methods,  
430 the look-up table defined in section 2.2 has been used except that a selection of the spectra  
431 described in section 5 has been performed before applying the GRSIR methodology. It  
432 has no interest to apply this selection to the  $k$ -NN methodology because in this selection,  
433 most of the spectra leading to multiple solutions for parameters are kept. The results,  
434 presented in Table 3, show that for most parameters, estimations are much more accurate  
435 with GRSIR. Only one parameter, the grain size of water ice, is better estimated on av-  
436 erage by  $k$ -NN. This may be due to the fact that too few values have been considered for  
437 simulations in the look-up table (only 5). In all other cases, we can see an important gain  
438 on the NRMSE which can be 3 times smaller with GRSIR than with  $k$ -NN. An illustra-  
439 tion of this gain is highlighted in Figure 7 which shows the scatter plot of the estimated  
440 proportions of CO<sub>2</sub> ice for both methods versus the real proportions. In this graphic, we

441 can notice that the range of variation of the estimated proportions of CO<sub>2</sub> ice is much  
442 larger with  $k$ -NN than with GRSIR. In fact, we can easily see, plotting the associated  
443 densities, that GRSIR reproduces better the density of the original proportions of CO<sub>2</sub> ice  
444 simulated in Tdata than  $k$ -NN (see figure 8). It is interesting to point out that  $k$ -NN does  
445 not give any information about the range of variation of the parameters of the test data  
446 and that estimations often vary in the same ranges of variation that the simulated values  
447 from the look-up table. On the other hand, GRSIR, as a first step, allows to evaluate in  
448 which ranges the parameters of an observed image are varying. Then a more appropriate  
449 look-up table can be built in the estimated ranges with a higher density of parameter val-  
450 ues. Applying GRSIR with this new extracted look-up table leads to even more accurate  
451 estimations given in Table 4. Finally, the SIRC, always close to 1, is very satisfying.

## 7. Retrieval of the physical parameters for the south polar cap of Mars

452 In this section, we present the first model inversions obtained by  $k$ -NN and GRSIR for  
453 hyperspectral images acquired by OMEGA during orbits 61, 103 and 41 (see section 2).  
454 The study of these images by  $k$ -NN and GRSIR leads to 30 different maps that we will not  
455 present in this paper but that can be found in the work of *Bernard-Michel et al.* [2007a].  
456 We draw up here the main conclusions.

457 The model inversion on the image observed from orbit 103 by GRSIR and  $k$ -NN shows  
458 that GRSIR gives very smooth mappings for all sets of parameters. Moreover, GRSIR  
459 estimations vary continuously while  $k$ -NN estimations assume a small number of values.  
460 An example is given in Figure 9, where we see that the proportion of dust is nearly al-  
461 ways estimated to a constant equal to 0.0003 with  $k$ -NN. With GRSIR, the map is more  
462 detailed. In the same way, figure 10 shows the proportion of dust estimated by  $k$ -NN and

463 GRSIR on the portion of the polar cap observed during orbit 41. With  $k$ -NN, estimations  
464 assume now 8 different values and seem to indicate that, at the very center of the bright  
465 cap, very few dust is observed. The abundance of dust increases significantly when getting  
466 closer from the boundaries. The estimated map with GRSIR is more detailed and leads  
467 to slightly different conclusions. In particular, the area presenting a poor proportion of  
468 dust is more extended than with  $k$ -NN. Nevertheless if, globally, maps are much smoother  
469 and detailed with GRSIR, they never differ entirely from  $k$ -NN's.

470 Another interesting remark concerns the estimation of the grain size of CO<sub>2</sub> ice in images  
471 61 and 103. In fact, images 61 and 103 represent approximately the same portion of the  
472 polar cap and should consequently give close estimations for each studied parameter. But  
473 we observed that estimations of the grain size of CO<sub>2</sub> ice are strongly different for both  
474 images and more especially with  $k$ -NN methodology (see figure 11). Observations 61 and  
475 103 were acquired approximately 12 Mars days apart during a period of the year when  
476 the solar illumination was declining over the south pole. Consequently, neither the state  
477 of the atmosphere (e.g. the dust content) nor the acquisition geometry by the sensor were  
478 strictly equivalent but likely comparable. These differences translate to small changes  
479 on the overall level of reflectance of the spectra and on the CO<sub>2</sub> ice bands intensity and  
480 shape. This is very much comparable to the introduction of noise in a relative sense be-  
481 tween observations 61 and 103. Since our remote sensing problem is partly ill-conditioned,  
482 a non regularized inversion method such as the  $k$ -NN will be much more sensitive to this  
483 noise than a regularized one such as the GRSIR. This is exactly what one can notice.  
484 The discrepancy that remains between the densities of the estimated grain sizes for orbit  
485 61 and 103 is mainly due to the conjugated effect of an increasingly grazing illumination

486 over a slightly dusty atmosphere that diminishes the spectral contrast of the observations.  
487 Such an effect was not taken into account in the modeling.

488 Finally, for the sake of validation, we compared estimated maps with the Wavanglet  
489 approach developed in [*Schmidt et al.*, 2007]. "Wavanglet" is a supervised automatic de-  
490 tection method that identifies in hyperspectral images spectral features and thus produces  
491 distribution maps of chemical compounds. It uses three steps: A. Selection of a library  
492 composed of reference spectra (the signature of the compounds to be detected); B. Appli-  
493 cation of a Daubechies wavelet transform to referenced spectra and determination of the  
494 wavelet subspace that best separates all referenced spectra; C. In this selected subspace,  
495 calculation of the spectral angle between each spectrum of an observation and a given ref-  
496 erence spectrum. In particular this angle, that we will denote the wavanglet angle, allows  
497 to quantify in a relative sense the spatial variations of the different compound abundances  
498 at the surface. We present in figure 12 the cosine of the wavanglet angle that makes each  
499 spectrum of the images 41 and 103 with a reference spectrum of martian dust. The closer  
500 it is from one, the greater the dust proportion is. We have a similar map for the water  
501 proportion. Globally, estimates of the latter quantities are more noisy with wavanglet  
502 than with GRSIR and k-NN, especially for the dust proportion but they generally are in  
503 agreement with some exceptions. For example, in the image observed during orbit 103,  
504 both *k*-NN and wavanglet methodologies display an area with strong proportion of dust  
505 in the lower right part of figure 12(B), that is absent with GRSIR. In order to see if  
506 this area really contains more dust than other areas, we selected the spectrum (denoted  
507 by A in figure 12) corresponding to the greatest proportion of dust. We compared it to  
508 two other spectra from the cap. The first spectrum (B) has been chosen in a pure CO<sub>2</sub>

509 area with very few dust. The second one (C) has been chosen in a area containing dust.  
510 According to  $k$ -NN and wavglet results, this area should however contain less dust than  
511 the area where we extracted spectrum A. The spectra A, B and C are presented in figure  
512 13. We can see that as, expected, the spectrum B is really different from the spectrum A.  
513 On the other hand, spectra A and C are really similar showing that the area of interest  
514 does not contain as much dust as the wavglet methodology predicts. On the opposite,  
515 estimations given by GRSIR are more coherent with this spectral analysis.

## 8. Conclusion

516 In this paper, we propose a regularized version of Sliced Inverse Regression in order  
517 to retrieve the physical parameters that best explain the spectra observed on Mars by  
518 the OMEGA imaging-spectrometer. To the best of our knowledge, this methodology  
519 has never been used in the domain of remote sensing and more particularly in planetary  
520 sciences. Results on simulations are promising showing that estimations are accurate  
521 and most of the time better than the ones given by the  $k$ -nearest neighbors algorithm.  
522 On a real data, maps are much smoother than with  $k$ -NN and seem to give a coherent  
523 mapping if we compare the inversion of different hyperspectral images of the same portion  
524 of surface of Mars. Moreover, GRSIR is a fast algorithm that calculates once and for all  
525 the relationship between spectra and parameters for a determined physical model. Thus,  
526 it is then really easy to inverse each new observed spectrum if it is coherent with the model.  
527 The main limit of GRSIR approach is that we currently do not give any uncertainties of our  
528 estimations when inverting a real image. We could calculate experimental uncertainties  
529 based on simulations, but it supposes that the noise in the spectra has been well evaluated.  
530 If not, uncertainties will probably be underestimated. Some improvements could also be

531 proposed to choose the regularization parameter and a more complete analysis of the  
532 influence of the noise in the GRSIR methodology would be interesting. A comparison  
533 with other training approaches such as SVM or neural networks would allow to better  
534 validate results. Finally, the development of a multivariate regularized GRSIR under  
535 constraint is conceivable in order to estimate proportions simultaneously.

536 **Acknowledgments.** This work is supported by a contract with CNES through its  
537 Groupe Système Solaire Program and by INRIA.

## References

- 538 Aster, R., B. Borchers, and T. C.H. (2005), *Parameter Estimation and Inverse Problems*,  
539 Elsevier Academic Press.
- 540 Bernard-Michel, C., S. Douté, L. Gardes, and S. Girard (2007a), Estimation of mars  
541 surface physical properties from hyperspectral images using sliced inverse regression,  
542 *Tech. rep.*, INRIA, <http://hal.inria.fr/inria-00187444/>.
- 543 Bernard-Michel, C., L. Gardes, and S. Girard (2007b), Gaussian regularized sliced inverse  
544 regression, *Tech. rep.*, INRIA, <http://hal.inria.fr/inria-00180496/>.
- 545 Bibring, J.-P., et al. (2004a), *OMEGA: Observatoire pour la Minéralogie, l'Eau, les Glaces*  
546 *et l'Activité*, pp. 37–49, ESA SP-1240: Mars Express: the Scientific Payload.
- 547 Bibring, J.-P., et al. (2004b), Perennial water ice identified in the south polar cap of mars,  
548 *Nature*, 428, 627–630.
- 549 Bishop, C. (2006), *Pattern Recognition and Machine Learning*, Springer.
- 550 Brown, R. H., et al. (2004), The Cassini Visual And Infrared Mapping Spectrometer  
551 (Vims) Investigation, *Space Science Reviews*, 115, 111–168, doi:10.1007/s11214-004-

553 Carlson, R., M. Anderson, R. Mehlman, and R. Johnson (2005), Distribution of hydrate  
554 on europa: Further evidence for sulfuric acid hydrate, *Icarus*, *177*(2), 461–471.

555 Carlson, R. W., P. R. Weissman, W. D. Smythe, J. C. Mahoney, the NIMS Science, and  
556 E. Teams (1992), Near infrared spectrometer experiment on Galileo, *Space Sci. Rev.*,  
557 *60*, 457–502.

558 Combal, B., F. Baret, M. Weiss, A. Trubuil, D. Macé, A. Pragnère, R. Myneni,  
559 Y. Knyazikhin, and L. Wang (2002), Retrieval of canopy biophysical variables from  
560 bidirectional reflectance using prior information to solve the ill-posed inverse problem,  
561 *Remote Sensing of Environment*, *84*, 1–15.

562 Douté, S., and B. Schmitt (1998), A multilayer bidirectional reflectance model for the anal-  
563 ysis of planetary surface hyperspectral images at visible and near-infrared wavelengths,  
564 *J. Geophys. Res.*, *103*(12), 31,367–31,390.

565 Douté, S., B. Schmitt, R. M. C. Lopes-Gautier, R. W. Carlson, L. Soderblom, and  
566 J. Shirley (2001), Mapping SO<sub>2</sub> frost on Io by the modeling of NIMS hyperspectral  
567 images, *Icarus*, *149*, 107–132.

568 Douté, S., E. Deforas, F. Schmidt, R. Oliva, and B. Schmitt (2007), A Comprehen-  
569 sive Numerical Package for the Modeling of Mars Hyperspectral Images, in *Lunar and*  
570 *Planetary Institute Conference Abstracts, Lunar and Planetary Institute Conference*  
571 *Abstracts*, vol. 38, p. #1836.

572 Douté, S., B. Schmitt, J.-P. Bibring, Y. Langevin, F. Altieri, G. Bellucci, B. Gondet, and  
573 the Mars Express Omega Team (2007), Nature and composition of the icy terrains from  
574 mars express omega observations, *Planetary and Space Science*, *55*, 113–133.

575 Douté, S., F. Schmidt, B. Schmitt, Y. Langevin, M. Vincendon, J.-P. Bibring, and Omega  
576 Team (2008), Physical Characterization of the South Seasonal Cap of Mars During  
577 Recession from OMEGA Observations, in *Lunar and Planetary Institute Conference*  
578 *Abstracts, Lunar and Planetary Inst. Technical Report*, vol. 39, p. #1736.

579 Durbha, S., R. King, and N. Younan (2007), Support vector machines regression for  
580 retrieval of leaf area index from multiangle imaging spectroradiometer, *Remote Sensing*  
581 *of Environment*, 107, 348–361.

582 Hapke, B. (1993), *Theory of reflectance and emittance spectroscopy*, Topics in Remote  
583 Sensing, Cambridge, UK: Cambridge University Press, 1993.

584 Kamgar-Parsi, B., and J. Gualtieri (1990), Solving inversion problems with neural net-  
585 works, *International Joint Conference on Neural Networks*, 3, 955–960.

586 Kimes, D., Y. Knyazikhin, J. Privette, A. Abuegasim, and F. Gao (2000), Inversion  
587 methods for physically-based models, *Remote Sensing Reviews*, 18, 381–439.

588 Li, K. (1991), Sliced inverse regression for dimension reduction, *Journal of the American*  
589 *Statistical Association*, 86, 316–327.

590 Mosegaard, K., and A. Tarantola (2002), Probabilistic approach to inverse problems,  
591 *International Handbook of Earthquake and Engineering Seismology (Part 1)*, pp. 237–  
592 265.

593 Murchie, S., et al. (2007), Compact reconnaissance imaging spectrometer for mars (crism)  
594 on mars reconnaissance orbiter (mro), *Journal of Geophysical Research (Planets)*,  
595 112(E11), E05S03, doi:10.1029/2006JE002682.

596 Philpot, W., et al. (2004), Bottom characterization from hyperspectral image data,  
597 *Oceanography*, 17(2), 76–85.

598 Pragnère, A., F. Baret, M. Weiss, R. Myneni, Y. Knyazikhin, and L. Wang (1999), Com-  
599 parison of three radiative transfer model inversion techniques to estimate canopy bio-  
600 physical variables from remote sensing data, *Geoscience and Remote Sensing Sympo-*  
601 *sium, 1999. IGARSS '99 Proceedings. IEEE 1999 International, 2*, 1093–1095.

602 Schmidt, F., S. Douté, and B. Schmitt (2007), WAVANGLET: An efficient supervised  
603 classifier for hyperspectral images, *Geoscience and Remote Sensing, IEEE Transactions*,  
604 *45*(5), 1374–1385.

605 Scholkopf, B., and A. J. Smola (2002), *Learning with Kernels: Support Vector Machines*,  
606 *Regularization, Optimization, and Beyond*, MIT Press, Cambridge, MA.

607 Shkuratov, Y., L. Starukhina, H. Hoffmann, and G. Arnold (1999), A model of spectral  
608 albedo of particulate surfaces: implications for optical properties of the moon, *Icarus*,  
609 *137*, 235–246.

610 Tarantola, A. (2005), *Inverse problem theory and model parameter estimation*, SIAM.

611 Weiss, M., F. Baret, R. Myneni, A. Pragnère, and Y. Knyazikhin (2000), Investigation of  
612 a model inversion technique to estimate canopy biophysical variables from spectral and  
613 directional reflectance data, *Agronomie 20*, pp. 3–22.

**Table 1.** Sampling strategy for the simulation of the look-up table. The range of variation is given for each varying parameter as well as the number of distinct values simulated.

Parameters	Look-up table		Test data
	range	# distinct values	range
Proportion of water	[0.0001 0.0029]	15	[0.0006 0.002]
Proportion of CO <sub>2</sub>	[0.9942 0.9998]	29	[0.996 0.9988]
Proportion of dust	[0.0001 0.0029]	15	[0.0006 0.002]
Grain size of water	[50 450]	5	[100 400 ]
Grain size of CO <sub>2</sub>	[30000 165000]	28	[40000 105000]

**Table 2.**  $k$ -NN estimates for spectra S1 and S2 (described in section 3)

Parameters	Spectrum S1		Spectrum S2	
	Real values	$k$ -NN	Real values	$k$ -NN
Proportion of water	0.0019	0.0021	0.0013	0.0029
Proportion of CO <sub>2</sub>	0.9969	0.9966	0.9969	0.9942
Proportion of dust	0.0012	0.0013	0.0017	0.0029
Grain size of water	156	150	109	150
Grain size of CO <sub>2</sub>	65721	60000	78993	45000

**Table 3.** Validation criteria calculated on Tdata with GRSIR and  $k$ -NN methodology.

Parameters	$k$ -NN	GRSIR	
		NRMSE	SIRC
Proportion of water	0.86	0.40	0.90
Proportion of CO <sub>2</sub>	0.88	0.30	0.98
Proportion of dust	0.44	0.17	0.99
Grain size of water	0.43	0.54	0.84
Grain size of CO <sub>2</sub>	0.53	0.22	0.95

**Table 4.** Validation criteria calculated on Tdata with GRSIR. Here the spectra that constitute the look-up table have been selected after a first inversion by GRSIR.

Parameters	GRSIR	
	NRMSE	SIRC
Proportion of water	0.27	0.92
Proportion of CO <sub>2</sub>	0.22	0.99
Proportion of dust	0.13	0.99
Grain size of water	0.37	0.92
Grain size of CO <sub>2</sub>	0.19	0.98

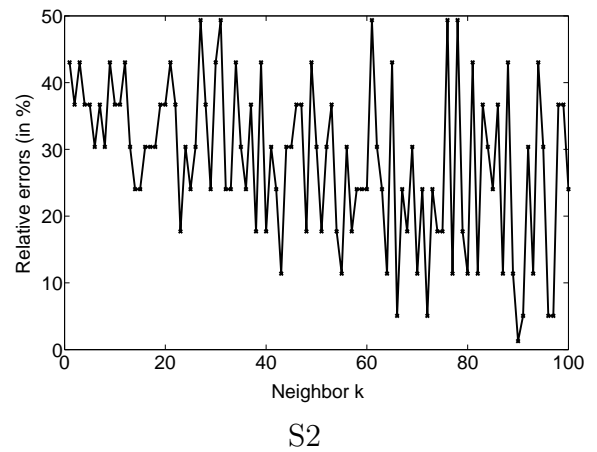
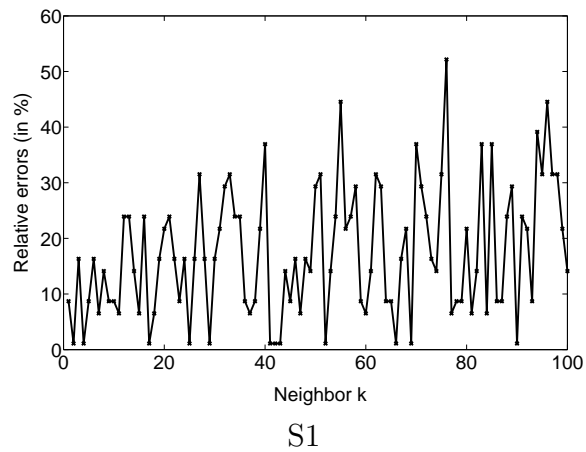


**Figure 1.** Relative errors on the grain size of CO<sub>2</sub> ice for the 100 nearest neighbors of spectra S1 and S2 in the lookup table. Horizontally:  $k$ th neighbor. Vertically: Relative errors on the grain size of CO<sub>2</sub> ice.

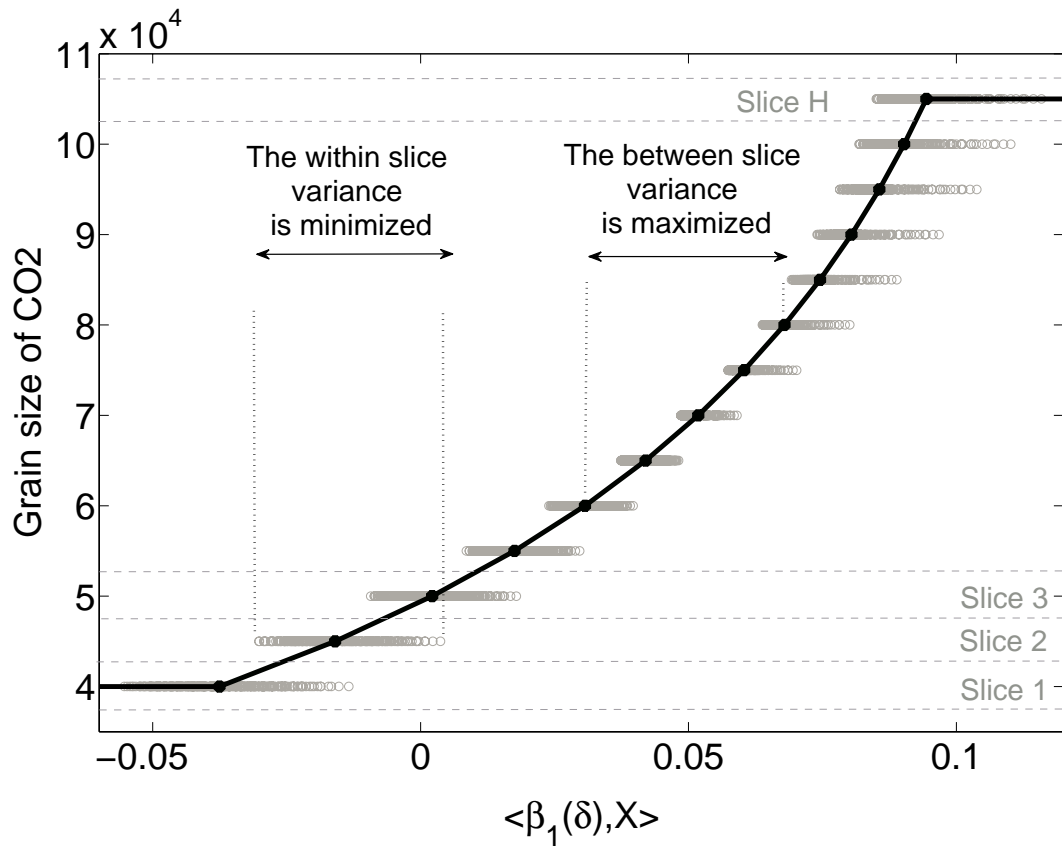


**Figure 2.** Functional relationship between reduced spectra on the first GRSIR axis and the grain size of CO<sub>2</sub> ice. This graphics illustrates the GRSIR methodology showing that the relationship is the best when the within slice variance is minimized or equivalently when the between slice variance is maximized. Horizontally: reduced spectra from the learning database on the first GRSIR axis. Vertically: Grain size of CO<sub>2</sub> ice.

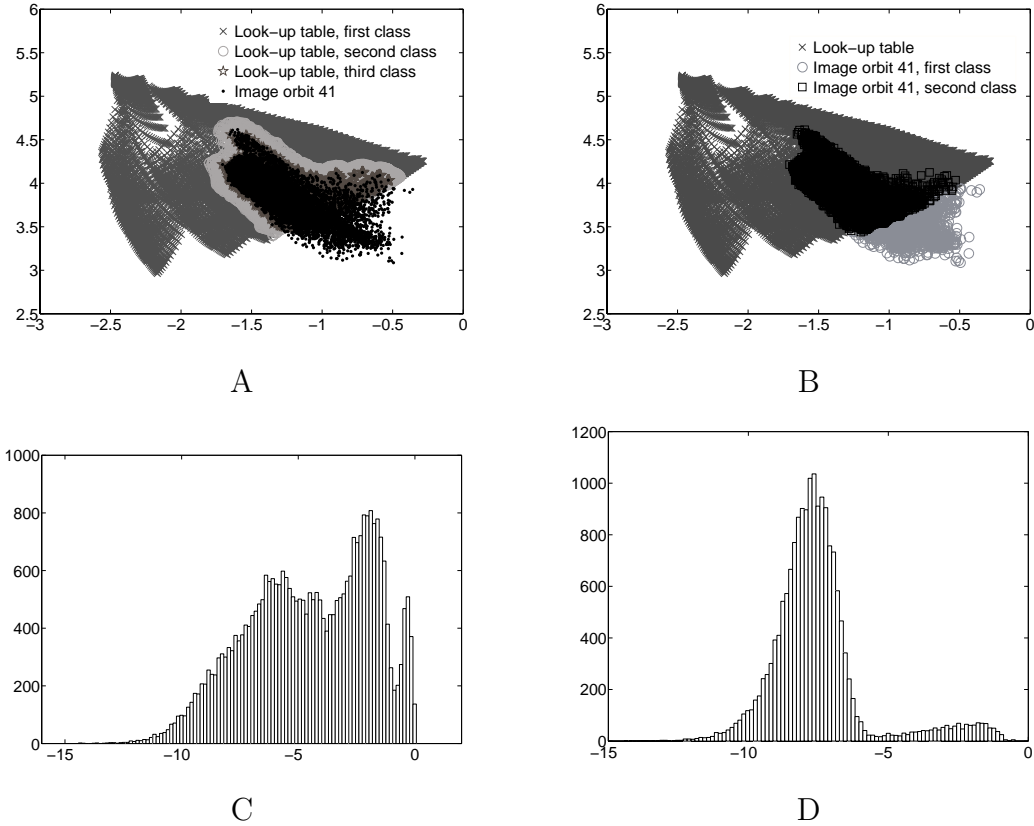


**Figure 3.** Selection of the “useful” spectra in the look-up table and of the “invertible” spectra in the observed data. A: Selection of a look-up table. Projections of the observed spectra from orbit 41 and the look-up table on the 2 first PCA axes (PCA applied to the look-up table). We distinguish 3 classes. The third class is the retained look-up table. B: Selection of invertible spectra in the image from orbit 41. The second class is retained for inversion. C: histogram of the distances between each spectrum of the look-up table and its nearest neighbor in the image from orbit 41. D: histogram of the distances between each spectrum of the image from orbit 41 and its nearest neighbor in the selected sub-look-up table.

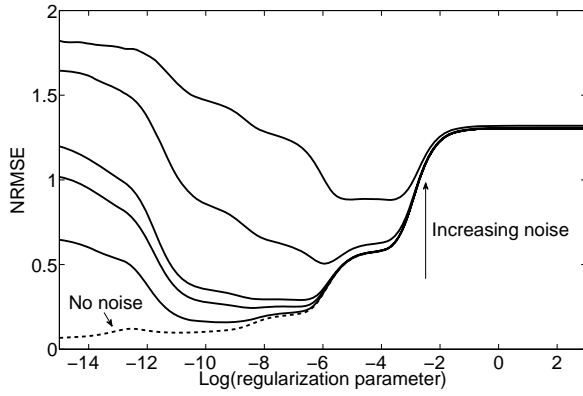


**Figure 4.** Influence of the noise in the choice of the regularization parameter. Horizontally: logarithm of the regularization parameter. Vertically: NRMSE for the grain size of  $\text{CO}_2$  ice. A multiGaussian noise has been introduced in the test data with a diagonal covariance  $C = \nu I_p$  proportional to the identity matrix  $I_p$ . The experience has been repeated five times with increasing values of  $\nu$ . One test has been also realized without any noise in the data.

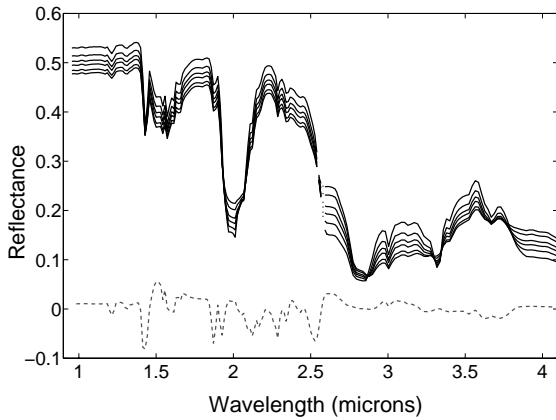


**Figure 5.** Plain line: series of spectra extracted from the lookup table for  $\text{CO}_2$  ice grain size varying between 30 and 165 millimeters, the other parameters being kept constant at mean values. Dotted-dash line: Componentwise multiplication between GRSIR axis for the grain size of  $\text{CO}_2$  ice and a representative spectrum (see section 6.4)

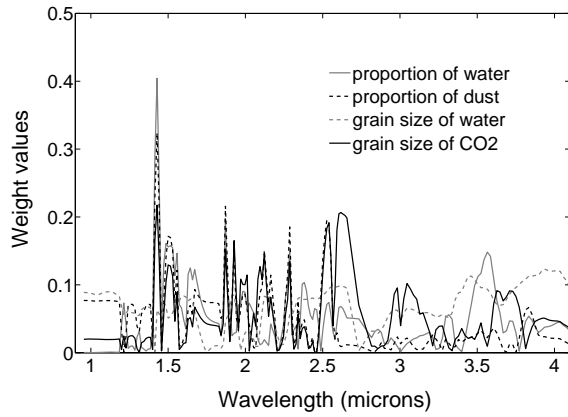


**Figure 6.** Horizontally: wavelengths. Vertically: GRSIR weights for the proportions of water ice and dust and the grain sizes of water and CO<sub>2</sub> ices.

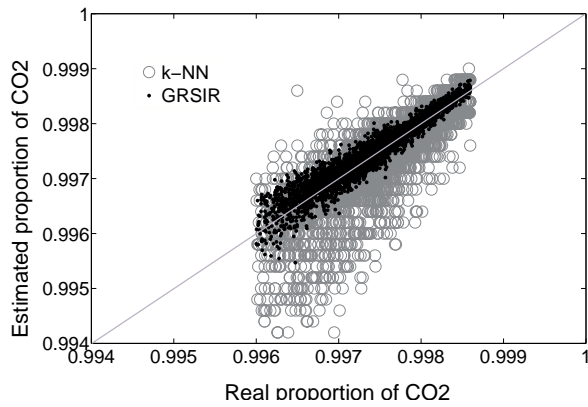


**Figure 7.** Scatter plot of the proportion of CO<sub>2</sub> ice from the test data versus estimated values. Horizontally: proportion of CO<sub>2</sub> ice. Vertically: estimated proportions of CO<sub>2</sub> ice by GRSIR and *k*-NN.

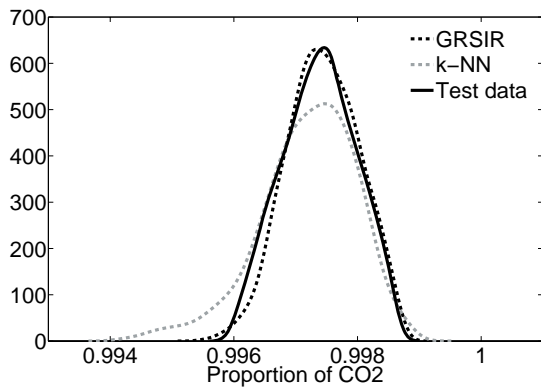


**Figure 8.** Density of the estimated proportions of CO<sub>2</sub> ice from the test data by  $k$ -NN and GRSIR compared to the density of real proportions.

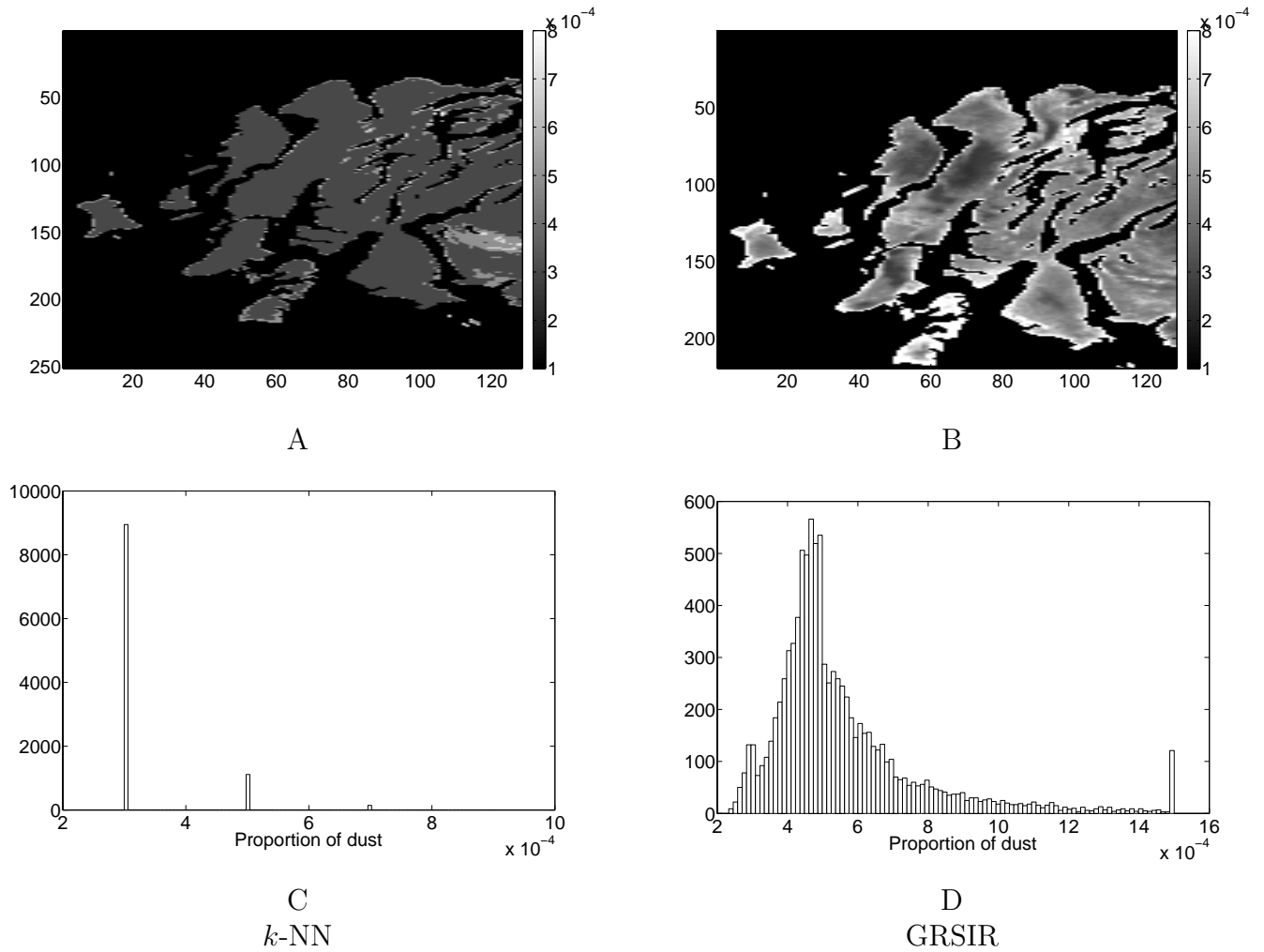


**Figure 9.** Proportion of dust estimated by  $k$ -NN (A) and GRSIR (B) from the hyperspectral image observed from orbit 103. The histograms of the estimations for the entire image are presented in (C) for  $k$ -NN and (D) for GRSIR.

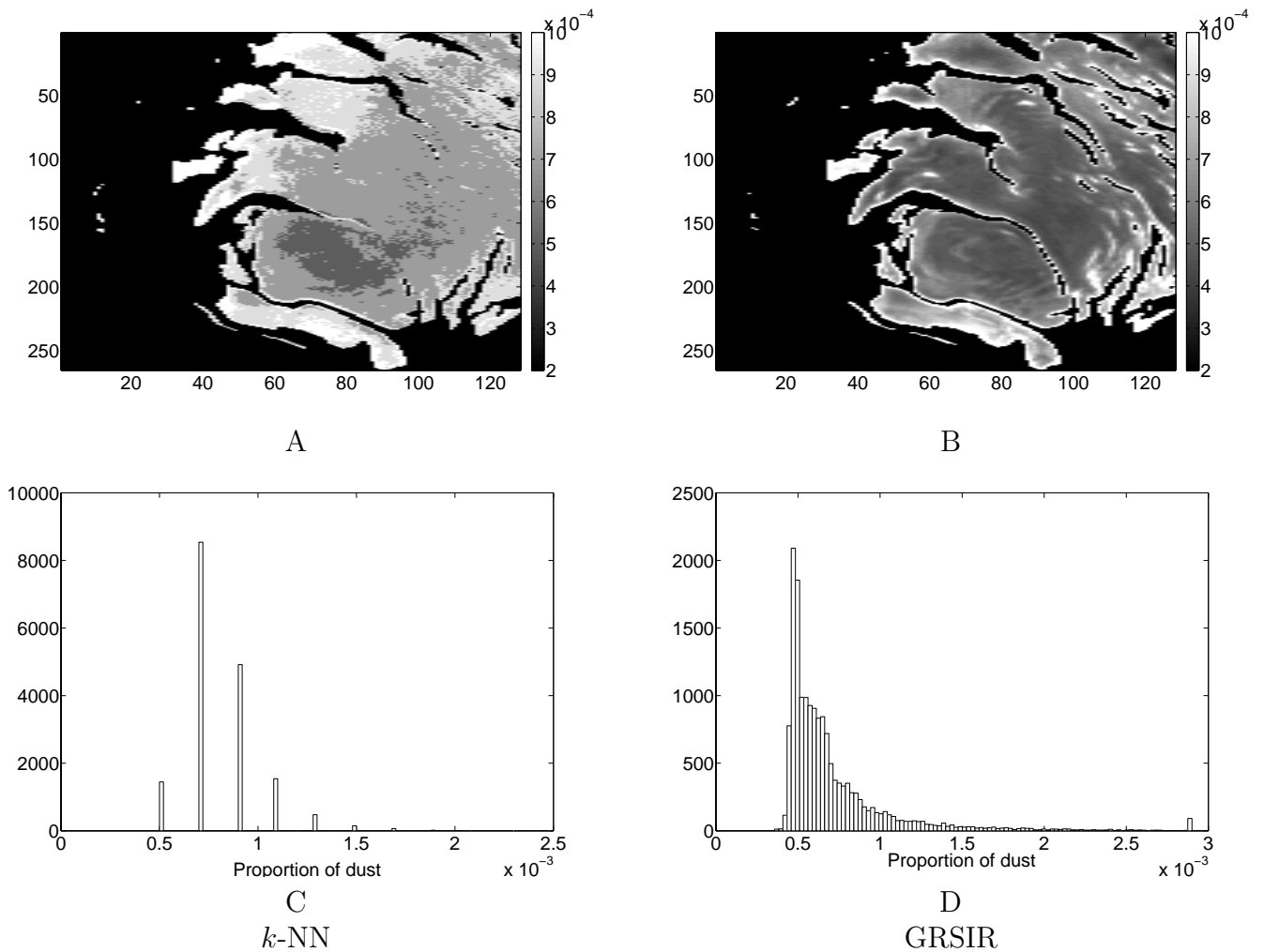


**Figure 10.** Proportion of dust estimated by  $k$ -NN (A) and GRSIR (B) from the hyperspectral image observed from orbit 41. The histograms of the estimations for the entire image are presented in (C) for  $k$ -NN and (D) for GRSIR.

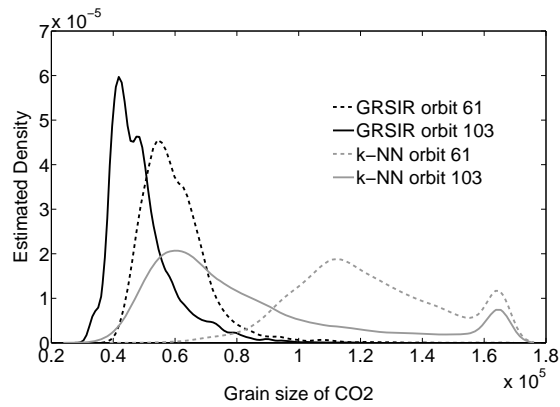


**Figure 11.** Comparison between the densities of the estimated grain sizes of CO<sub>2</sub> ice by *k*-NN and GRSIR in images from orbit 61 and 103.

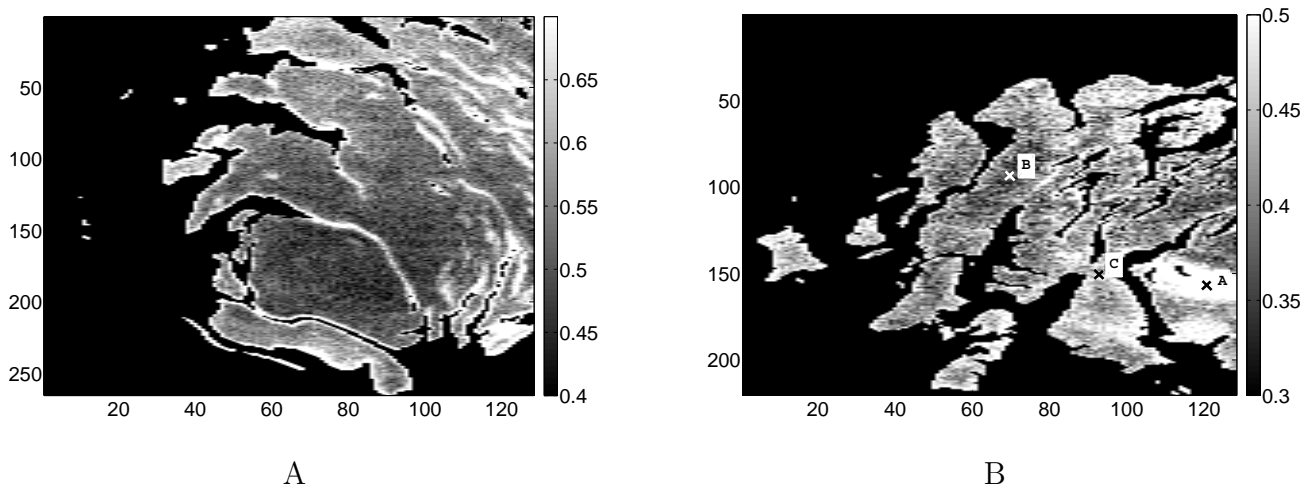


**Figure 12.** Cosinus of the Wavanglet angle between the observed spectra and a reference spectrum of martian dust for the hyperspectral images acquired during orbit 41 (A) and during orbit 103 (B).

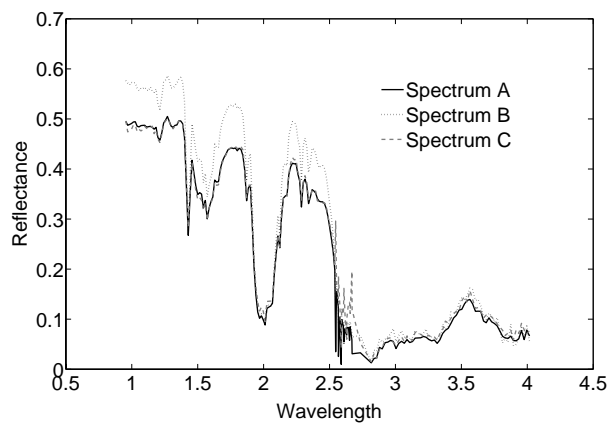


**Figure 13.** Spectra extracted from the locations labelled A, B and C in the image 103 of figure 12 (B)